Journal of Materials Chemistry C

ROYAL SOCIETY OF CHEMISTRY

PAPER

View Article Online
View Journal | View Issue

Cite this: J. Mater. Chem. C, 2024, 12, 5766

A novel selenophene based non-fullerene acceptor for near-infrared organic photodetectors with ultra-low dark current †‡

Zhuoran Qiao, [a] Qiao He, [a] Alberto D. Scaccabarozzi,[b] Julianna Panidi, [a] Adam Marsh,[c] Yang Han,[d] Polina Jacoutot,[a] Davide Nodari,[a] Tianyi Zhang,[a] Amirah Way,[e] Andrew J. P. White,[a] Thomas D. Anthopoulos, [c] Wing Chung Tsoi, [e] Artem A. Bakulin, [a] Martin Heeney, *[ac] Zhuping Fei *[f] and Nicola Gasparini *[a]

Received 18th December 2023,
Accepted 8th March 2024

DOI: 10.1039/d3tc04678h

rsc.li/materials-c

Near-infrared organic photodetectors (OPDs) have great potential in many applications. However, the high dark current of many OPD devices tends to limit their specific detectivity and overall performance. Here we report a novel non-fullerene acceptor (IDSe) based on an alkylated indacenodiselenophene core, with extended light absorption up to 800 nm. When blended with the donor polymer PTQ10, we obtained OPD devices with an exceptionally low dark current density of 1.65 nA cm^{-2} at −2 V, high responsivity and specific detectivity exceeding 10^{12} Jones at 790 nm. The superior properties of PTQ10:IDSe devices are related to the higher and more balanced charge carrier mobility compared to the analogous thiophene based blend (PTQ10:IDIC). We also demonstrate large area PTQ10:IDSe based devices by doctor blade in air with a record low dark current of 1.2×10^{-7} A cm^{-2} under −2 V bias.

Introduction

Photodetectors (PDs) play a paramount role in sensing fields such as imaging, environmental monitoring, and machine vision to convert light into electrical signals.[1] Despite the excellent device performance,[2,3] commercial PDs feature high intrinsic brittleness and complicated manufacturing processes, which leads to high costs and limit the application in large-area flexible imagers. As a result, in the past few years, photodetectors based on organic materials have received increasing attention. Compared with inorganics, organic photodetectors (OPDs) use lightweight, flexible materials and offer potentially low fabrication costs, while having promising photogeneration

Nicola Gasparini

Dr Nicola Gasparini received his BSc and MSc, in Chemistry and Organic Chemistry, and Photochemistry and Molecular Materials, respectively, from the University of Bologna, Italy. In 2014 he joined the group of Professor Brabec in the Institute of Materials for Electronics and Energy Technology (i-MEET) at the Friedrich Alexander University Erlangen-Nürnberg (FAU) and received his PhD in 2017. In September 2017, he joined the King Abdullah University of Science and Technology (KAUST) as a postdoctoral fellow. In September 2019, he moved to the Department of Chemistry of Imperial College London as an independent researcher holding the Imperial College Research Fellowship. In early 2022, Nicola was appointed Lecturer in Chemistry (assistant professor, tenured) in the Department of Chemistry. His research interests are in organic and perovskite semiconductors, with particular interests in charge transport and recombination processes in solar cells and photodetectors.

[a] Department of Chemistry and Centre for Processable Electronics, Imperial College London, London W12 0BZ, UK. E-mail: n.gasparini@imperial.ac.uk, m.heeney@imperial.ac.uk
[b] Center for Nano Science and Technology, Politecnico di Milano, Istituto Italiano di Tecnologia, Raffaele Rubattino 81, Milano 20134, Italy
[c] King Abdullah University of Science and Technology (KAUST), KAUST Solar Center (KSC), Thuwal 23955, Saudi Arabia
[d] School of Materials Science and Engineering and Tianjin Key Laboratory of Molecular Optoelectronic Science, Tianjin University, Tianjin 300350, China
[e] SPECIFIC, Faculty of Science and Engineering, Swansea University, Bay Campus, Fabian Way, Swansea SA1 8EN, UK
[f] Institute of Molecular Plus, Tianjin Key Laboratory of Molecular Optoelectronic Science, Tianjin University, Tianjin 300072, China. E-mail: zfei@tju.edu.cn

† Electronic supplementary information (ESI) available. See DOI: https://doi.org/10.1039/d3tc04678h

‡ Amirah way could not be contacted to confirm the final author list prior to acceptance.

yield.[4–7] Moreover, by fine-tuning the optical bandgap of the organic material, OPDs can be engineered for high and specific light detection. In terms of the fabrication environment, OPDs can be processed from solution by employing different coating techniques ranging from spin coating, spray coating and doctor blading under ambient conditions.[2] Depending on the wavelength of interest, organic photodetectors can be employed for ultraviolet, visible and near-infrared applications. The latter is useful for night-vision cameras, health monitoring and light communication technologies.[6,8–11]

To maximize the light-to-current conversion, the active layer in OPD devices generally consists of a blend of electron-donating and electron-accepting organic semiconductor materials. The past few years have experienced the development of the so-called non-fullerene acceptors (NFAs), which overcome some of the intrinsic limitations of traditional fullerene and its derivatives, such as weak light absorption, limited energy-level tuning and blend instability. Small molecule NFAs show numerous attractive features, including high purity, crystallinity and lower reorganizational energy.[12–16] Furthermore, the bandgap and energy levels can be readily tuned by varying the synthetic structure in order to achieve near-infrared light absorption.[17–20]

Numerous NFAs have been reported to date, with a popular design motif based on an electron-rich donor (D) core being flanked by two electron-deficient acceptor (A) units, the so-called A–D–A system. Analyzing the structures of reported NFAs, it is clear that many of the best performing contain thiophene-based fused aromatics within the donor core.[21] This is likely due to a combination of factors, such as the well-developed chemistry of thiophene which facilitates their synthesis, as well as the diffuse orbitals of the sulfur heteroatom which may benefit intermolecular charge transport. An elegant strategy to shift the absorption windows >750 nm consists of replacing the thiophene moiety with selenophene. Selenophene has lower aromatic stabilization energy than thiophene, and the replacement of thiophene with selenophene in conjugated oligomers or polymers has been shown to increase the quinoidal character of the material, resulting in a reduced band gap and a red-shifted absorption.[22–25] Furthermore, the larger, more polarisable Se atom can enhance the intermolecular interactions resulting in improved charge carrier mobility.[26,27]

Until now, few fused selenophene containing NFAs have been reported to date and to the best of our knowledge, all of those reported have contain aryl-based solubilizing groups at the bridgehead carbons.[23,28–35] Although the aryl group affords good solubility to the NFA, we and others have recently demonstrated that the replacement of the alkylaryl groups with simple straight chain alkyl groups resulted in significant changes in the solid-state microstructure of thiophene-based NFAs and an overall enhancement in their power conversion efficiency (PCE) for organic solar cells.[36–38] Encouraged by this observation, we report here the first preparation of a NFA containing a fused indacenodiselenophene with octyl sidechains at the bridgehead positions. This is the direct selenophene analogue of the previously indacenodithiophene acceptor known as IDIC, widely reported in the OPV community.[39–41] We that note that IDIC typically uses hexyl sidechains, rather than octyl, but the octyl derivative has been reported with very similar properties to the hexyl derivative. In addition, analysis of the single crystal structures demonstrates similar packing of the conjugated cores for both sidechains.[42,43]

In this work, we show that the selenophene analogue exhibits a red-shifted absorption compared to the thiophene analogue, and when paired with a suitable wide band gap donor, organic photodetector devices using donor–acceptor bulk heterojunction configuration have an ultralow dark current density (J_d) of 1.65 nA cm^{-2} at −2 V and a specific detectivity (D^*) of 10^{12} Jones at −2 V. In addition, higher and balanced carrier mobility is observed in the blend containing selenophene analogue compared to the thiophene benchmark. We also fabricated large-area OPDs (5 × 5 cm substrates) using doctor blade coating in air, a more scalable technique than spin-coating, and obtained low dark current density of 1.2×10^{-7} A cm^{-2} at −2 V.

Results and discussion

Synthesis and characterization

The synthesis of IDSe is shown in Scheme 1 and starts from our previously reported 2,7-bis(trimethylsilyl)-4,9-dihydro-*s*-indaceno[1,2-*b*:5,6-*b*′]bis(selenophene).[44] Treatment with six equivalents of sodium tert-butoxide followed by 1-bromooctane resulted in a one-pot alkylation and desilyation, and subsequent bromination with NBS afforded compound **3** in a yield of 62% over the two

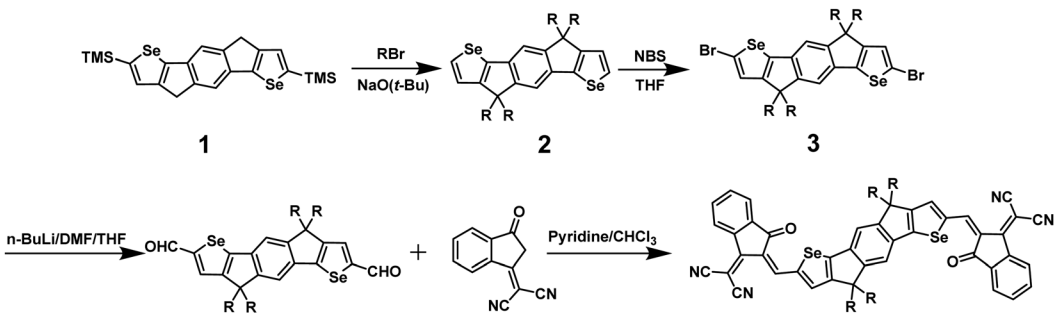

Scheme 1 Synthetic route to IDSe.

steps. Treatment of **3** with *n*-BuLi in THF at −100 °C, followed by the addition of dry DMF afforded the dialdehyde **4** in 85% yield. We note that performing the lithiation at higher temperatures resulted in a considerable amount of decomposition, presumably by the ring opening of the selenophene following deprotonation at the alpha position. The final acceptor molecule IDSe was prepared by the Knoevenagel condensation reaction of **4** and 1,1-dicyanomethylene-3-indanone (IC) in 87% yield.

The new acceptor showed good solubility in common organic solvents and was characterized by a combination of NMR and mass spectroscopy. A crystal of IDSe was successfully grown by slowly diffusing methanol into a solution of IDSe in dichloromethane at room temperature, and was analyzed by single-crystal X-ray diffraction, as shown in Fig. 1, with the crystallographic data are summarized in the (ESI†). The alkyl chains on the bridging carbons have been removed to aide visualization, but the full structure is shown in Fig. S1 (ESI†), with the octyl sidechains extending away from the backbone in a fully *trans* (or anti) conformation with two *gauche* defects. The IDSe shows a nearly planar conjugated backbone with a centre of symmetry at the middle of the benzene ring on IDSe unit, and a slight twist of 12.6° between the IDSe core and the IC endgroup, slightly smaller than the analogous IDIC (14.9°).[45] Interestingly, the distance between Se and O atoms is around 2.71 Å, which is much shorter than their van der Waals radius (3.42 Å), indicating a non-covalent interaction which helps to lock the molecule in a single conformation. Analysis of the crystal packing (Fig. 1c and d) demonstrates that the molecules are arranged in a two-dimensional grid-like packing, with two parallel lines of molecules intersecting *via* the overlap of the IC endgoups. There is a strong overlap of the IC endgroups, with an interplanar distance of 3.46–3.50 Å, similar to IDIC. The voids in the structure shown in Fig. 1d are filled by residual solvent and the octyl sidechains. Such a packing arrangement forms an extended three dimensional packing arrangement that may be beneficial for exciton and charge transport. Analysis of spun-cast thin-films of both IDIC and IDSe by 2D GIWAXS (Fig. 1e and f) and scattering profiles (Fig. S11, ESI†) shows that both materials exhibit clear diffraction features along the vertical and horizontal directions. However, the IDSe appears more ordered than IDIC, both in terms of intensity and richness of the diffractions, for films of similar thickness.

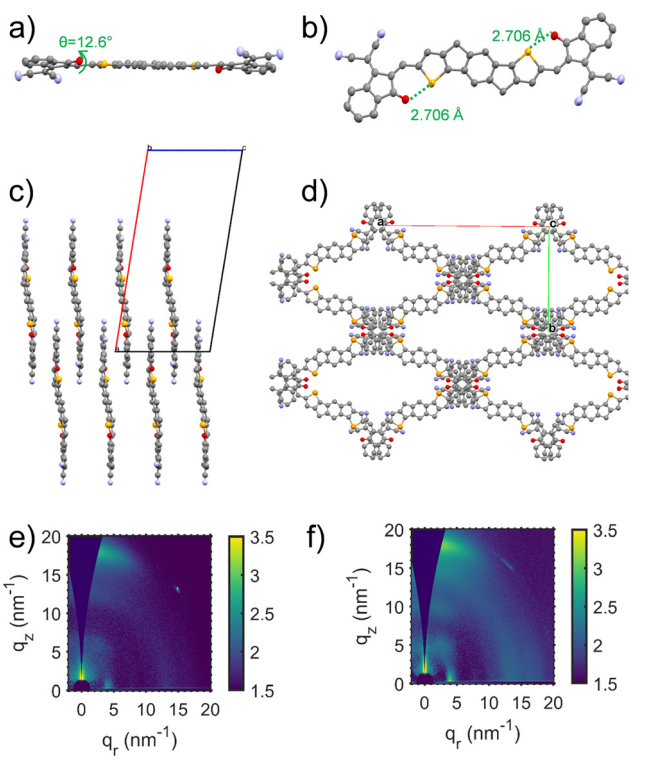

Fig. 1 (a) Side and (b) front-view of IDSe crystal structure (alkyl sidechains removed for clarity) and the packing diagrams of IDSe project along the (c) *b*-axis and (d) *c*-axis showing close overlap of end-groups. 2D GIWAXS images of films of (e) IDIC and (f) IDSe.

Thermogravimetric analysis indicated that IDSe has excellent thermal stability, with a decomposition temperature above 350 °C at 5% weight loss (Fig. S2, ESI†). Examination of the thermal behaviour by differential scanning calorimetry (DSC) demonstrated that IDSe exhibits two distinct melting peaks at 191 and 225 °C in the first heating cycle but forms a glass upon cooling (Fig. S3, ESI†). Upon subsequent heating, the glass undergoes two exothermic crystallization transitions at 130 and 156 °C, followed by a main endothermic melting transition at 210 °C in the second heating cycle. This behaviour is repeated in the third heating/cooling cycle.

IDSe exhibits an absorption maximum at 685 nm with a shoulder peak around 630 nm in dilute chlorobenzene solution with a high absorption coefficient (e) of 1.77 × 10^5 M^{-1} cm^{-1} (Fig. S4, ESI†). In thin film, the absorption maximum is significantly red-shifted to 749 nm and the film absorbs strongly in the region from 600 to 800 nm, with an absorption edge at 800 nm corresponding to an optical band gap of 1.55 eV. In comparison to the reported thiophene analogue with hexyl sidechains (IDIC), changing to selenophene results in a red shift of 33 nm in the solid state and 21 nm in solution. The energy alignments of the IDSe in the solid state were evaluated *via* Photoelectron Spectroscopy in Air (PESA) measurements and cyclic voltammetry (PESA and CV, Fig. S5, ESI†) on a Pt working electrode. From the ionisation potential measured with PESA, the highest occupied molcule orbital (HOMO) energies of PTQ10, IDSe and IDIC were estimated as −5.20 eV, −5.79 eV and −5.81 eV, respectively. Whereas their lowest unoccupied molecular orbital (LUMO) were estimated adding the optical bandgap to the HOMO values. CV measurements allowed a direct measurement of the reduction (and oxidation) potentials, and demonstrated a similar trend to the PESA, albeit with different values. Thus, HOMO and LUMO levels of −5.70 eV and −3.92 eV were estimated for IDSe, and −5.74 eV and −3.90 eV for IDIC by reference to the ferrocene/ferrocenium couple with a HOMO of −4.8 eV. The HOMO is slightly upshifted compared to the thiophene analogue (IDIC), as is often observed in selenophene containing materials.[22]

Recently various NFA materials have demonstrated promising performance in thin-film transistor devices.[46–49] Therefore we

investigated the charge carrier behaviour of both acceptors in organic thin films transistors (OTFTs) fabricated in a bottom-contact, top-gate device architecture to evaluate holes and electrons mobility. For hole mobility measurements the source and drain electrodes were treated with a self-assembled monolayer in order to reduce the workfunction, whereas for electron mobility no surface treatments were performed.

Representative transfer and output characteristics of IDIC and IDSe OTFTs are presented in Fig. S6 and S7 (ESI†), where it can be seen that both materials show ambipolar behaviour, with IDSe having lower turn-on voltage and better overall performance. IDSe showed more than one order of magnitude higher charge carrier mobility than IDIC, with values of 0.16 and 0.22 $cm^2\ V^{-1}\ s^{-1}$ for electrons and holes in the saturation regime, respectively, *versus* values of 0.002 and 0.009 $cm^2\ V^{-1}\ s^{-1}$ for IDIC devices.

The higher charge carrier mobility of IDSe can be related to a combination of the more diffuse and polarizable Se orbitals,[26,27] in combination with the more ordered packing and the overall higher crystallinity as observed from the GIWAXS measurements (Fig. 1).[50]

We fabricated organic photodetectors by blending IDSe with the p-type donor material PTQ10 for their complementary absorption and cascade energy alignment for efficient light-to-current conversion.[51] The chemical structures of PTQ10 and the NFAs used and their absorption spectra are reported in Fig. 2a and b. Moreover, PTQ10 has been proven to be suitable for a thick active layer which is helpful to reduce dark current.[52] The OPDs were fabricated in an inverted architecture consisting of ITO/ZnO/active layer/MoO_3/Ag. Various fabrication parameters including solution concentration, donor–acceptor ratio, active layer thickness, thermal annealing temperature were carefully optimized. The current density–voltage (*J–V*) characteristics were measured both under light and in the dark conditions. Devices based on PTQ10:IDSe delivered ultra-low dark current density of 1.65×10^{-9} A cm^{-2} at −2 V, whereas PTQ10:IDIC showed a J_d of 4.67×10^{-8} A cm^{-2} at −2 V. The J_d values obtained in IDSe based OPDs are one of the lowest dark currents reported for NIR OPDs to the best of our knowledge.[5]

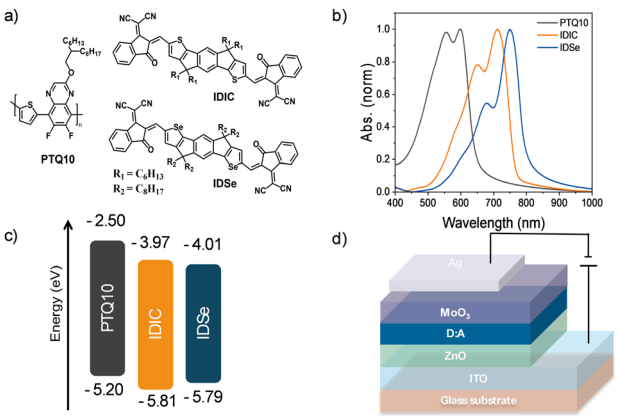

Fig. 2 (a) Chemical structures of PTQ10, IDIC and IDSe; (b) normalized absorbance of the neat materials; (c) energy levels of the materials extracted from PESA measurements; (d) schematic of the BHJ donor–acceptor device structure with inverted architecture.

To fully understand the performance of OPDs further characterizations were conducted on both PTQ10:IDIC and PTQ10:IDSe devices. First, external quantum efficiency (EQE) was measured under different bias and converted into responsivity (R) using equation $R = EQE\frac{q}{h\nu}$. A 50 nm red-shift of responsivity is observed in PTQ10:IDSe devices, in agreement with the smaller band gap of IDSe, demonstrating the potential of selenophene based acceptors to promote near-infrared light detection.

To compare different PD devices, the most common figure of merit is the specific detectivity (D^*), defined as $D^* = \frac{R\sqrt{A * B}}{I_n}$, where R is the responsivity, A is the device area, B is noise measurement bandwidth, and I_n Is the noise current.[53] The noise spectrum was measured through a low noise amplifier and the results show that the PTQ10:IDSe device depicts a lower noise current spectral density level of 1×10^{-12} A $Hz^{-1/2}$ when compared to 3×10^{-12} A $Hz^{-1/2}$ of PTQ10:IDIC devices (Fig. 4a). The 1/*f* corner frequency,[54] which is defined as the crossover point of 1/*f* noise and the broadband noise, also presents a different profile for two blends. The PTQ10:IDIC-based OPDs have a much higher frequency transition corner, indicating much higher flicker-noise dominating behaviour in the lower frequency area. The comparison of detectivity is plotted in Fig. 3c, indicating OPDs based on PTQ10:IDSe have a similar detectivity level in the visible light region and a higher detectivity into the NIR region, due to the extended absorption of IDSe.

Photodetectors are expected to be operated at different light intensity depending on their application. For this reason we measured the *J–Vs* under different light conditions (Fig. S8, ESI†) and calculated the linear dynamic range (LDR).[5,52,55] LDR is determined as the ratio between the maximum and the minimum photocurrent density ($J_{ph} = J_l - J_d$, where J_l and J_d refer to the current density at light and dark environment, respectively.) according to the equation $\mathrm{LDR} = 20 \times \log\frac{J_{ph,max}}{J_{ph,min}}$. Plotted in Fig. 3d, PTQ10:IDSe delivered a 120 dB LDR compared to 80 dB for PTQ10:IDIC devices at −2 V. This result can be attributed to the lower dark current and noise current of the IDSe blend, which are helpful to maintain the linear light response and outperform IDIC under low light conditions.

Apart from the detection range, operating speed is of great importance when assessing the performance of a NIR OPD.[56,57] Frequency response, which measures the frequency at which the photocurrent value drops to −3 dB, is a key figure of merit.[58] The overall operating frequency is either limited by the charge carrier transient time or by the RC property of the intrinsic circuits which gives rise to the equation $f_{-3dB}^{-2} = f_{tr}^{-2} + f_{RC}^{-2}$, where f_{tr} is the carrier transient time-limited frequency and f_{RC} is the RC time constant-limited frequency.[59] Fig. 4b depicts the −3 dB cutoff frequency of 60 kHz and 220 kHz for OPDs based on PTQ10:IDIC and PTQ10:IDSe blends, respectively. For modern video applications, 10 kHz is a benchmark for fast

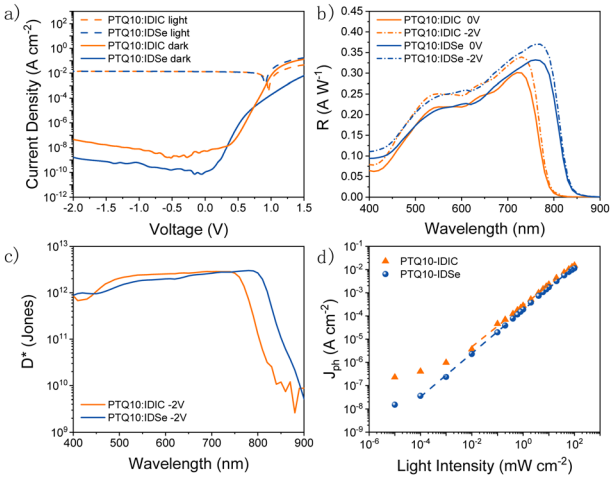

Fig. 3 (a) Current density–voltage characteristics of PTQ10:IDIC and PTQ10:IDSe OPDs under dark and AM1.5G illumination; (b) responsivity and (c) specific detectivity of the OPD devices under negative bias applied; (d) linear dynamic range at −2 V for PTQ10:IDIC and PTQ10:IDSe under white light illumination.

speed detection.[56] Therefore, both blend combinations are competitive candidates for fast speed OPDs. To further understand the charge carrier transient characteristics, the rise and fall dynamics are investigated by illumination with a high-frequency continuous square-wave LED. Fig. 4c shows the rise and fall time of both devices. The rise time represents the time-interval for the signal to respond between 10% and 90% of the maximum value, and the *vice versa* for fall time.[60] PTQ10:IDSe exhibited slightly faster transient time characteristics than PTQ10:IDIC devices, as summarized in Table 1. Rise and fall times are dependent on the mobility, recombination and extraction processes of charge carriers, which indicate faster mobility and efficient recombination processes might play significant roles.

In order to explain the possible reason for the low dark current and excellent NIR performance of OPDs based on PTQ10:IDSe blend, charge carrier mobility was measured using the steady-state space-charge limited current (SCLC) method. Hole-only (glass/ITO/PEDOT:PSS/active layer/MoO_3/Ag) and electron-only (glass/ITO/ZnO/active layer/DPO/Ag) devices were fabricated and measured. The *J*–*V* plot of single-carrier devices (Fig. S9, ESI†) was fitted using equation $J = \frac{9}{8}\varepsilon\varepsilon_0\mu_0\frac{(V-V_{bi})^2}{L^3}\exp\left(0.89\gamma\sqrt{\frac{V-V_{bi}}{L}}\right)$ where the ε represents the material relative dielectric constant (assumed to have a value of 3), ε_0 indicates the vacuum permittivity and μ_0 is the mobility at zero-field. V_{b_i} is the built-in potential, L is the thickness of the active layer measured by the profilometer, γ is the field activation factor of mobility.[61] For field-dependent diffusion, the result extracted from the previous equation was brought into the Poole–Frenkel expression which can be written as $\mu = \mu_0\exp(\gamma\sqrt{E})$. The values of hole and electron mobility were calculated for a field of 5×10^{-4} V cm^{-1} corresponding to a potential of 0.5 V across a 100 nm thick film.

The pristine NFA materials depicted an electron mobility of 4.3×10^{-4} cm^2 V^{-1} s^{-1} and 1.2×10^{-4} cm^2 V^{-1} s^{-1} for IDSe and

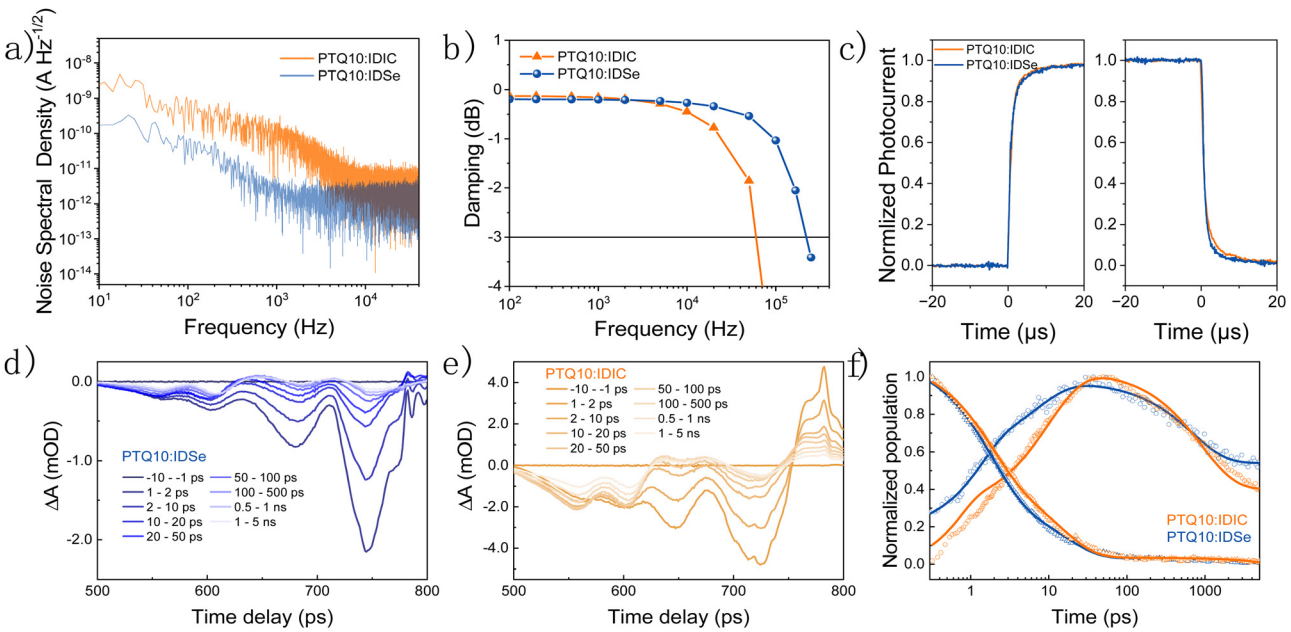

Fig. 4 (a) Noise current spectral density, (b) cut-off frequency and (c) transient photocurrent measurements at −2 V for IDSe and IDIC-based OPD. Visible TA spectra for (d) PTQ10:IDSe blend and (e) PTQ10:IDIC blend films at different pump–probe delay times. Both samples were excited at 700 nm with a fluence of 2 μJ cm^{-2}. (f) Deconvoluted kinetics of excitons (triangles) and charges (circles) in PTQ10:IDIC (orange) and PTQ10:IDSe (blue). Solid lines are monoexponential fittings of the decay and rise dynamics.

Table 1 Photodetectors figures of merit and mobility values of the IDSe and IDIC based devices

	R (A W^{-1})	LDR (dB)	D^* (Jones)	Rise time (μs)	Fall time (μs)	$\mu_{sclc(e)}$ (cm^2 V^{-1} s^{-1})	$\mu_{sclc(h)}$ (cm^2 V^{-1} s^{-1})
PTQ10:IDIC	0.35 (730 nm)	80	2.86×10^{12}	3.6	7.0	2.1×10^{-5}	1.6×10^{-5}
PTQ10:IDSe	0.37 (770 nm)	120	3.02×10^{12}	3.3	5.5	1.3×10^{-4}	1.3×10^{-4}

IDIC, respectively. The higher SCLC mobility calculated for IDSe is in line with that observed for the OTFT devices. As expected upon blending the NFAs with the donor polymer, the electron mobility for both acceptors drops, but to a lesser degree for IDSe. Thus electron and hole mobility for PTQ10:IDSe are equivalent at 1.3×10^{-4} cm^2 V^{-1} s^{-1}, respectively, whereas PTQ10:IDIC afforded electron and hole mobilities of 2.1×10^{-5} cm^2 V^{-1} s^{-1} and 1.6×10^{-5} cm^2 V^{-1} s^{-1}. These results indicate that in the PTQ10:IDSe blend both hole and electron mobility are higher and more balanced (1.00 μ_h/μ_e ratio) than that in PTQ10:IDIC blend (0.76 μ_h/μ_e ratio). The balanced electron/hole mobility is effective for suppressing bimolecular recombination, which translates to lower dark current level.[62]

Examination of the blend morphology with GIWAXS demonstrates that both films exhibit similar microstructure (Fig. S10 and S11, ESI†), with clear diffraction peaks assignable to both the polymer and NFA crystallites. No obvious differences were apparent, suggesting that the higher charge mobility stemming from the replacement of thiophene with selenophene is the principal reason for the better OPD performance.

Next, we further examine the underlying exciton and charge dynamics in these two systems using ultrafast transient absorption spectroscopy. Fig. 4d and e compares the visible time-resolved spectra of the two OPD blends. In both blends, the acceptor was selectively excited with 700 nm pump at low fluence, thereby taking care to avoid exciton–exciton and exciton–charge annihilation events which dominate early recombination and dissociation dynamics. In the IDSe-based blend, the initial peak at 745 nm is assigned to the IDSe exciton. This initial peak is present in the neat IDSe TA spectra in Fig. S12b (ESI†) and is assigned to ground state absorption (GSB) of the acceptor. From the neat IDSe measurements, we extract an exciton lifetime of 26 ps, which is comparable with previously reported lifetimes of IDIC excitons.[63]

It is, however, apparent from the evolution of the blend spectra in time that other spectral components dominate at later times. Namely, we observe a slower decay of the GSB peaks at 560 and 604 nm in both blends, which we attribute to PTQ10 based on its neat TA data presented in Fig. S12a (ESI†). Furthermore, both blends demonstrate a clear growth of a positive photoinduced absorption (PIA) signal around 620–740 nm for IDSe blend and around 620–680 nm for the IDIC blend. Given the strong spectral overlap of the GSB and PIA features from D/A domains, we performed global analysis of the TA data for both blends. The results are deconvoluted spectra (Fig. S13, ESI†) of individual excited state species in the blend with their associated dynamics. The kinetic traces of the two spectral components are presented in Fig. 4f. Since we selectively excited the acceptor, we assign the decaying component to the IDSe and IDIC exciton (blue and orange triangles, respectively), while any later signal evolution is attributed to charge transfer states and free polaron formation. IDSe blend exhibits a 2 ps rise of the charge component, which subsequently decays within 710 ps. Analogous components in the IDIC blend resulted in 3 ps exciton decay accompanied by 3 ps charge generation, which then decayed within 820 ps. The PTQ10:IDIC excited state dynamics are in good agreement with a previously reported spectroscopic study.[63] Overall, both blends exhibit fast exciton quenching and subsequent charge generation within 2–3 ps. While IDSe blend generates charges marginally faster, both blends exhibit efficient charge generation, which could be linked to high crystallinity of both blends, which tends to favour unbound charge transfer states over bound ones, which more readily generate free charges.[64]

Finally we tested PTQ10:IDSe devices under bias-stress in the dark to investigate their stability. The results indicates that PTQ10:IDSe devices have an excellent stability, maintaining the ultra-low dark current density of 6.30 nA cm^{-2} and LDR of 100 dB after 92 hours of continuous bias applied (Fig. S14 and S15 (ESI†), respectively). For real-world applications, spin coating is not feasible for large-area coating techniques. For this reason, we fabricated OPD devices on 5 × 5 cm ITO substrates by blade coating PTQ10:IDSe in air with an active area of 0.3 cm^{-2}. The OPD devices delivered a dark current density of 1.2×10^{-7} A cm^{-2} under −2 V bias (Fig. 5a). Despite the higher J_d value compared to the small-area devices, which can be attributed to a non-homogenous coating of the active layer on large substrates and in air, this low value can be ranked among the top low dark current for large-area devices according

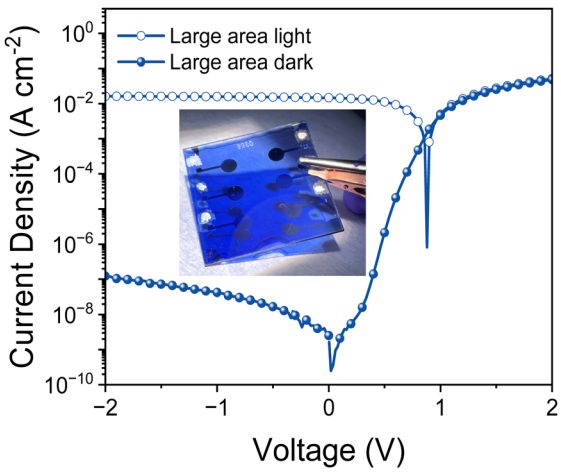

Fig. 5 (a) Current–voltage characteristics of large-area PTQ10:IDSe-based devices under AM1.5G illumination and dark; in inset the picture of the large-area device (5 × 5 cm substrates).

to the reported literature.[65,66] These results indicate the high potential of chalcogen engineering as a strategy to develop high performing blends for OPD devices.

Conclusion

In conclusion, we report a new non-fullerene acceptor IDSe based on an indacenodiselenophene core functionalized with linear alkyl chains. This is the direct selenium analogue of the well known thiophene based acceptor IDIC, and to the best of our knowledge is the first indacenodiselenophene based NFA not containing aryl groups at the bridgehead positions. The replacement of sulfur with selenium results in a red-shift of the resulting acceptor, with an absorption extending 800 nm. X-ray analysis of IDSe single crystal shows an intermolecular non-covalent interaction between Se and O, and pronounced intramolecular interactions between the indanone endgroups. Thin film transistors of IDSe exhibit ambipolar behaviour, with balanced hole and electron transport that is over one order of magnitude higher than IDIC.

Vis-NIR light-detecting organic photodetectors were fabricated with IDSe and its thiophene analogue IDIC from blends with the polymer donor PTQ10. OPDs based on the IDSe blend featured a J_d of 1.65×10^{-9} A cm^{-2} together with R of 0.37 A W^{-1} and D^* of 3×10^{12} Jones at 790 nm wavelength under -2 V bias. The ultralow J_d gives rise to an excellent 120 dB LDR under light illumination. While IDSe blend generates charges marginally faster than PTQ10:IDIC, their higher and balanced charge carried mobility values explain the lower dark current and superior optoelectronic performance. PTQ10:IDSe OPDs demonstrated outstanding stability under continuous -2 V bias in the absence of light. Finally we fabricated devices on 5 × 5 cm substrates by blade coating with an active area of 0.3 cm^2, showcasing a record low J_d of 1.2×10^{-7} A cm^{-2} at -2 V bias, proving that PTQ10:IDSe blend has the ability to be applied in mass production in the future. These results demonstrate that alkylated indacenodiselenophene cores form promising building blocks for the fabrication of near-IR absorbing acceptors exhibiting high crystallinity.

Experimental

Synthesis and characterization

The synthetic route is outlined in Scheme 1 and described in further detail in the ESI.† Details of synthetic and characterization equipment and procedures can be found in the ESI.†

Device fabrication

Organic photodetectors. PTQ10:IDIC and PTQ10:IDSe organic photodetectors were fabricated in the cleanroom using inverted structure (glass/ITO/ZnO/active layer/MoO_3/Ag). The indium tin oxide (ITO, 15 Ω sq^{-1}) was pre-patterned on the glass substrates (12 mm × 12 mm). The substrates were firstly cleaned by sonication in acetone for 10 min, followed by detergent and deionized water. After another 10 min sonication in acetone, the substrates were cleaned by isopropanol and then immediately transferred into a vacuum environment for 8 min oxygen plasma treatment. A 40 nm thickness ZnO layer was deposited on the ITO by 4000 rpm, 40 s spin-coating using a zinc acetate dihydrate precursor solution (219 mg zinc acetate dihydrate precursor dissolved in 60.4 μl 1-ethanolamine and 2 ml 2-methoxyethanol) followed by annealing at 180 °C for 10 min. The ZnO coated substrates were transferred into a dry nitrogen glove box (<0.1 ppm H_2O, <0.1 ppm O_2). The active layer solutions were obtained by dissolving donor PTQ10 (purchased from brilliant matters) with acceptor IDIC (purchased from 1-material – organic nano electronic) and IDSe (see ESI† for synthesis details) in chloroform (CF). The donor and acceptor were blended in a 1 : 1.5 ratio (wt/wt) in a 25 mg ml^{-1} concentration. The solutions were stirred overnight in the glove box at room temperature and heated to 40 °C 20 min before spin-coating to make sure materials were completely dissolved. The active layer solution was coated on the ZnO from the warm solution using a spin coater, under the nitrogen atmosphere, at different spin speeds ranging from 1000 rpm to 3000 rpm for 40 s. The active layers were then transferred onto a programmable heat plate in the glove box for 140 °C, 5 min thermal annealing (TA) treatment. For the thermal evaporation, a 10 nm MoO_3 and a 100 nm Ag layer was sequentially deposited. The MoO_3 layer was deposited at a 0.15 Å s^{-1} rate and in terms of Ag layer, deposition speed ranged from 0.5 Å s^{-1} to 1 Å s^{-1}. Through a shadow mask, the area for each pixel is 0.045 cm^2.

For the large-area devices, ITO-coated glass substrates (5 cm × 5 cm) were cleaned following the identical procedure as that of small-area devices. ZnO was uniformly deposited on the ITO by spin coating, forming a layer with 40 nm thickness. The active layer solution of PTQ10:IDSe was prepared using the same concentration and donor–acceptor ratio compared to the solution for small-area devices. The doctor blade coater (ZAA 2300 Automatic film applicator, Zehntner) was pre-heated to 40 °C by a temperature controller before fabrication. The gap between ZnO surface and the doctor blade was set to 400 μm while the coating speed ranged from 20 mm s^{-1} to 60 mm s^{-1}. The substrates were continuously cleaned by the nitrogen gun until the start of coating. After doctor blade coating, 10 nm MoO_3 and 100 nm Ag were thermally evaporated onto the active layer which was covered by a special mask. The J–V performance of large-area devices between -2 V to 2 V bias under light condition was measured under the standard AM1.5 solar simulator where both electrodes were linked to a Keithley 2400 source meter by alligator clips. Dark current was measured with aluminum foil covering the devices in order to create a completely dark environment.

OTFTs fabrication. Bottom-contact, top-gate (BC-TG) were glass substrates. Substrates were cleaned in Decon 90/DI water solution for 5 min in sonication, followed by sequential sonication in acetone and isopropanol. 40 nm of gold were deposited *via* thermal evaporation in high vacuum (10^{-6} mbar) with the use of shadow masks to form the source/drain electrodes resulting transistor devices with channel length in the range

of 30–100 nm and width 1 mm. No further treatment was conducted for the electron-only devices. The TFTs were spin coated from 5 mg ml^{-1} solution in anhydrous chlorobenzene at 2000 rpm for 30 s, followed by annealing at 100 °C for 10 min. 900 nm of CYTOP were used as dielectric layer followed by 50 nm of thermal evaporated aluminum which formed the gate electrode. Device fabrication and electrical measurements were performed in a nitrogen glovebox. Transistor characterization was carried out using an Keithley 4200 semiconductor parameter analyzer.

Characterizations

***J–V* measurements.** *J–V* characteristics were measured using a Keithley 4200 Source-Measure unit (scan rate 25 mV s^{-1}). An Oriel Instruments Solar Simulator with a Xenon lamp and calibrated to a silicon reference cell was used to provide AM1.5G irradiance. For determination of the Linear Dynamic Range (LDR), white light LED driven by a function generator (ThorLabs DC2200) was used. The LED light was attenuated using a selection of neutral density filters placed between the lamp and OPD. The photocurrent (J_{ph}) was calculated as the difference in response between the illuminated current density (J_{light}) and dark current density (J_d) at each light intensity. All the devices were tested in nitrogen atmosphere.

Responsivity. Responsivity was measured using an integrated system from Quantum Design PV300. All the devices were tested in ambient air.

Dynamic measurements. Dynamic measurements were performed using a digital oscilloscope (Tektronix TDS3032B). The OPDs were illuminated with a neutral white light LED driven by a function generator (ThorLabs DC2200). For determination of the rise and fall time a 1 kHz square wave pulse was applied to the LED using the function generator. For determination of the cut-off frequency sinusoidal functions with varying frequencies between 100 Hz and 100 kHz were used to drive the LED connected to a FEMTO-100 preamplifier. All the devices were tested in nitrogen atmosphere.

Charge carrier mobility measurement. The mobility of each pristine material and blends was measured using steady-state space-charge limited current (SCLC) method. In order to make sure device electrodes can inject the desired charge carrier while blocking the carrier with different polarity, hole-only (glass/ITO/PEDOT:PSS/active layer/MoO_3/Ag) and electron-only (glass/ITO/ZnO/active layer/DPO/Ag) devices were fabricated. Devices were placed in the sample chamber and then measured in the dark from 0 V to 6 V under nitrogen environment.

Grazing incidence wide angle scattering (GIWAXS) measurements. GIWAXS measurements were performed at the non-crystalline diffraction beamline (BL11-NCD-Sweet) at ALBA Synchrotron Radiation Facility in Barcelona (Spain). A detector (Rayonix, WAXS LX255-HS) with a resolution of 1920 × 5760 pixels was used to collect the scattering signals. Sample holder position was calibrated with chromium oxide (Cr_2O_3) standard. The incident energy was 12.4 eV and the sample-to-detector distance was set at 200.93 mm. The angle of incidence αi was set between 0.1–0.15 and the exposure time was 5 s. 2D-GIWAXS patterns were corrected as a function of the components of the scattering vector with a Matlab® script developed by Aurora Nogales and Edgar Gutiérrez. Thin films were cast onto highly doped silicon substrates following same processing route used for the device fabrication.

Photoelectron spectroscopy in air measurements. PESA was recorded using a Riken Keiki PESA spectrometer (Model AC-2) with a power setting of 10 nW and a power number of 0.33. Samples for PESA were prepared on glass substrates.

Transient absorption spectroscopy. A broadband femtosecond transient absorption spectrometer Helios (Spectra Physics, Newport Corp.) was used for pump–probe measurements on the neat donor and acceptor films and their blends. A 1 kHz Ti:Sapphire regenerative amplifier (Solstice, Spectra Physics, Newport Corp.) delivered ultrafast laser pulses (800 nm, <100 fs FWHM) to an optical parametric amplifier (TOPAS Prime, Spectra Physics) and a frequency mixer (Niruvis, Light Conversion) to generate pump pulses at 700 nm, which were modulated at 500 Hz by an optical chopper system (Thorlabs). 800 nm seed pulses were also delayed on the 6 ns mechanical delay stage and passed through a sapphire crystal to produce a white light probe (400–900 nm). Spatial and temporal overlap of focused pump and probe beams was achieved on the thin film samples, contained in a quartz cuvette under a constant flow of nitrogen. The fluences were calculated based on the probe beam size of 0.5 mm^2 at the sample. Background and chirp corrections were applied to the spectra post-measurement using the Surface Xplorer software. Global analysis was performed using a genetic algorithm, originally written by Simon Gélinas.[67]

Author contributions

Z. Q., Z. F., M. H and N. G. conceived and developed the ideas. Z. Q. designed the experiment, fabricated and characterised the OPD devices under the supervision of N. G. Q. H., Y. H, A. W. synthesised the materials under the superivsion of M. H., W. C. T. and Z. F. J. P., T. Z., and D. N. helped with the electrical characterisations. P. J. performed ultra-fast characterisations under the superivision of A. A. B. A. D. S. performed GIWAXS measurements under the supervision of T. D. A., A. J. P. W. performed XRD measurements. Z. Q., N. G. wrote the manuscript. All authors commented on the manuscript.

Conflicts of interest

There are no conflicts to declare.

Acknowledgements

The authors thank the Engineering and Physics Science Research Council (EPSRC) (EP/T028513/1 and EP/V057839/1), the King Abdullah University of Science and Technology (KAUST) Office of Sponsored Research (OSR) under Award No. OSR-2020-CRG8-4095 and ORFS-2023-OFP-5544, NSG Pilkington, the M2A funding from the European Social Fund through the Welsh

Government. We are grateful to the SPECIFIC Innovation and Knowledge Centre (EP/N020863/1). A.D.S would like to thank the ALBA synchrotron (BL11 NCD-SWEET beamline) and staff, in particular Dr Eduardo Solano, for their help with the GIWAXS measurements.

References

1 P. C. Y. Chow and T. Someya, *Adv. Mater.*, 2020, **32**, 1902045.
2 C. Xie, X. T. Lu, X. W. Tong, Z. X. Zhang, F. X. Liang, L. Liang, L. B. Luo and Y. C. Wu, *Adv. Funct. Mater.*, 2019, **29**, 1806006.
3 Y. Xu and Q. Lin, *Appl. Phys. Rev.*, 2020, **7**, 11315.
4 Y. Z. Wang, J. Kublitski, S. Xing, F. Dollinger, D. Spoltore, J. Benduhn and K. Leo, *Mater. Horiz.*, 2022, **9**, 220–251.
5 G. Simone, M. J. Dyson, S. C. J. Meskers, R. A. J. Janssen and G. H. Gelinck, *Adv. Funct. Mater.*, 2019, **30**, 1904205.
6 F. P. García de Arquer, A. Armin, P. Meredith and E. H. Sargent, *Nat. Rev. Mater.*, 2017, **2**, 16100.
7 T. Y. Zhang, M. Moser, A. D. Scaccabarozzi, H. Bristow, P. Jacoutot, A. Wadsworth, T. D. Anthopoulos, I. McCulloch and N. Gasparini, *J. Phys. – Mater.*, 2021, **4**, 045001.
8 X. Liu, Y. Lin, Y. Liao, J. Wu and Y. Zheng, *J. Mater. Chem. C*, 2018, **6**, 3499–3513.
9 Z. Wu, Y. Zhai, H. Kim, J. D. Azoulay and T. N. Ng, *Acc. Chem. Res.*, 2018, **51**, 3144–3153.
10 P. Jacoutot, A. D. Scaccabarozzi, T. Y. Zhang, Z. R. Qiao, F. Aniés, M. Neophytou, H. Bristow, R. Kumar, M. Moser, A. D. Nega, A. Schiza, A. Dimitrakopoulou-Strauss, V. G. Gregoriou, T. D. Anthopoulos, M. Heeney, I. McCulloch, A. A. Bakulin, C. L. Chochos and N. Gasparini, *Small*, 2022, **18**, 2200580.
11 P. Jacoutot, A. D. Scaccabarozzi, D. Nodari, J. Panidi, Z. R. Qiao, A. Schiza, A. D. Nega, A. Dimitrakopoulou-Strauss, V. G. Gregoriou, M. Heeney, C. L. Chochos, A. A. Bakulin and N. Gasparini, *Sci. Adv.*, 2023, **9**, eadh2694.
12 J. Hou, O. Inganäs, R. H. Friend and F. Gao, *Nat. Mater.*, 2018, **17**, 119–128.
13 G. Y. Zhang, J. B. Zhao, P. C. Y. Chow, K. Jiang, J. Q. Zhang, Z. L. Zhu, J. Zhang, F. Huang and H. Yan, *Chem. Rev.*, 2018, **118**, 3447–3507.
14 C. Q. Yan, S. Barlow, Z. H. Wang, H. Yan, A. K. Y. Jen, S. R. Marder and X. W. Zhan, *Nat. Rev. Mater.*, 2018, **3**, 18003.
15 A. Armin, W. Li, O. J. Sandberg, Z. Xiao, L. M. Ding, J. Nelson, D. Neher, K. Vandewal, S. Shoaee, T. Wang, H. Ade, T. Heumüller, C. Brabec and P. Meredith, *Adv. Energy Mater.*, 2021, **11**, 2003570.
16 Q. He, P. Kafourou, X. T. Hu and M. Heeney, *SN Appl. Sci.*, 2022, **4**, 247.
17 A. Wadsworth, M. Moser, A. Marks, M. S. Little, N. Gasparini, C. J. Brabec, D. Baran and I. Mcculloch, *Chem. Soc. Rev.*, 2019, **48**, 1596–1625.
18 H. W. Cheng, Y. P. Zhao and Y. Yang, *Adv. Energy Mater.*, 2022, **12**, 2102908.
19 W. Gao, F. R. Lin and A. K. Y. Jen, *Sol. RRL*, 2022, **6**, 2100868.
20 X. T. Hu, Z. R. Qiao, D. Nodari, Q. He, J. Asatryan, M. Rimmele, Z. L. Chen, J. Martin, N. Gasparini and M. Heeney, *Adv. Opt. Mater.*, 2023, 2302210.
21 J. Y. Wang and X. W. Zhan, *Acc. Chem. Res.*, 2021, **54**, 132–143.
22 A. V. Marsh and M. Heeney, *Polym. J.*, 2023, **55**, 375–385.
23 B. Fan, F. Lin, X. Wu, Z. Zhu and A. K.-Y. Jen, *Acc. Chem. Res.*, 2021, **54**, 3906–3916.
24 G. C. Hoover and D. S. Seferos, *Chem. Sci.*, 2019, **10**, 9182–9188.
25 S. Y. Ye, V. Lotocki, H. Xu and D. S. Seferos, *Chem. Soc. Rev.*, 2022, **51**, 6442–6474.
26 Y. H. Wijsboom, A. Patra, S. S. Zade, Y. Sheynin, M. Li, L. J. W. Shimon and M. Bendikov, *Angew. Chem., Int. Ed.*, 2009, **48**, 5443–5447.
27 M. Al-Hashimi, Y. Han, J. Smith, H. S. Bazzi, S. Y. A. Alqaradawi, S. E. Watkins, T. D. Anthopoulos and M. Heeney, *Chem. Sci.*, 2016, **7**, 1093–1099.
28 H. Yu, Z. Y. Qi, J. Q. Zhang, Z. Wang, R. Sun, Y. Chang, H. L. Sun, W. T. Zhou, J. Min, H. Ade and H. Yan, *J. Mater. Chem. A*, 2020, **8**, 23756–23765.
29 H. Feng, X. L. Meng, L. Y. Fu, C. B. Liu, X. X. Yin, E. W. Zhu, Z. F. Li and G. B. Che, *J. Mater. Chem. C*, 2023, **11**, 3020–3029.
30 C. Yang, Q. S. An, H. R. Bai, H. F. Zhi, H. S. Ryu, A. Mahmood, X. Zhao, S. W. Zhang, H. Y. Woo and J. L. Wang, *Angew. Chem., Int. Ed.*, 2021, **60**, 19241–19252.
31 C. Labanti, M. J. Sung, J. Luke, S. Kwon, R. Kumar, J. S. Hong, J. Kim, A. A. Bakulin, S. K. Kwon, Y. H. Kim and J. S. Kim, *ACS Nano*, 2021, **15**, 7700–7712.
32 X. Liu, X. Jiang, K. F. Wang, C. Y. Miao and S. M. Zhang, *Materials*, 2022, **15**, 23.
33 J.-L. Wang, K.-K. Liu, L. Hong, G.-Y. Ge, C. Zhang and J. Hou, *ACS Energy Lett.*, 2018, **3**, 2967–2976.
34 Z. Liang, M. Li, X. Zhang, Q. Wang, Y. Jiang, H. Tian and Y. Geng, *J. Mater. Chem. A*, 2018, **6**, 8059–8067.
35 Y. Li, L. Zhong, F.-P. Wu, Y. Yuan, H.-J. Bin, Z.-Q. Jiang, Z. Zhang, Z.-G. Zhang, Y. Li and L.-S. Liao, *Energy Environ. Sci.*, 2016, **9**, 3429–3435.
36 Q. He, M. Shahid, X. Jiao, E. Gann, F. D. Eisner, T. Wu, Z. Fei, T. D. Anthopoulos, C. R. McNeill and M. Heeney, *ACS Appl. Mater. Interfaces*, 2020, **12**, 9555–9562.
37 Z. H. Luo, T. L. Xu, C. E. Zhang and C. L. Yang, *Energy Environ. Sci.*, 2023, **16**, 2732–2758.
38 Z. Fei, F. Eisner, X. Jiao, M. Azzouzi, J. Röhr, Y. Han, M. Shahid, A. Chesman, C. Easton, C. McNeill, T. Anthopoulos, J. Nelson and M. Heeney, *Adv. Mater.*, 2018, **30**, 1705209.
39 Y. Lin, Q. He, F. Zhao, L. Huo, J. Mai, X. Lu, C.-J. Su, T. Li, J. Wang, J. Zhu, Y. Sun, C. Wang and X. Zhan, *J. Am. Chem. Soc.*, 2016, **138**, 2973–2976.
40 Y. Li, N. Zheng, L. Yu, S. Wen, C. Gao, M. Sun and R. Yang, *Adv. Mater.*, 2019, **31**, 1807832.
41 Y. Lin, F. Zhao, S. K. K. Prasad, J. D. Chen, W. Cai, Q. Zhang, K. Chen, Y. Wu, W. Ma, F. Gao, J. X. Tang, C. Wang, W. You, J. M. Hodgkiss and X. Zhan, *Adv. Mater.*, 2018, **30**, 1706363.

42 Y. Zhang, Z. X. Liu, T. Shan, Y. Wang, L. Zhu, T. Li, F. Liu and H. L. Zhong, *Mater. Chem. Front.*, 2020, **4**, 2462–2471.
43 X. J. Li, H. Huang, I. Angunawela, J. D. Zhou, J. Q. Du, A. Liebman-Pelaez, C. H. Zhu, Z. J. Zhang, L. Meng, Z. Q. Xie, H. Ade and Y. F. Li, *Adv. Funct. Mater.*, 2020, **30**, 1906855.
44 Z. Fei, Y. Han, E. Gann, T. Hodsden, A. S. R. Chesman, C. R. Mcneill, T. D. Anthopoulos and M. Heeney, *J. Am. Chem. Soc.*, 2017, **139**, 8552–8561.
45 J. F. Qu, H. Chen, J. D. Zhou, H. J. Lai, T. Liu, P. J. Chao, D. N. Li, Z. Q. Xie, F. He and Y. G. Ma, *ACS Appl. Mater. Interfaces*, 2018, **10**, 39992–40000.
46 M. I. Nugraha, R. E. A. Ardhi, D. Naphade, W. M. Zhang, Y. Y. Yuan, M. Heeney and T. D. Anthopoulos, *J. Mater. Chem. C*, 2023, **11**, 12941–12948.
47 A. F. Paterson, R. P. Li, A. Markina, L. Tsetseris, S. MacPhee, H. Faber, A. H. Emwas, J. Panidi, H. Bristow, A. Wadsworth, D. Baran, D. Andrienko, M. Heeney, I. McCulloch and T. D. Anthopoulos, *J. Mater. Chem. C*, 2021, **9**, 4486–4495.
48 H. Bristow, K. J. Thorley, A. J. P. White, A. Wadsworth, M. Babics, Z. Hamid, W. M. Zhang, A. F. Paterson, J. Kosco, J. Panidi, T. D. Anthopoulos and I. McCulloch, *Adv. Electron. Mater.*, 2019, **5**, 1900344.
49 E. Gutierrez-Fernandez, A. D. Scaccabarozzi, A. Basu, E. Solano, T. D. Anthopoulos and J. Martín, *Adv. Sci.*, 2022, **9**, 2104977.
50 H. Tang, C. Yan, S. Karuthedath, H. Yin, Y. Gao, J. Gao, L. Zhang, J. Huang, S. So, Z. Kan, F. Laquai, G. Li and S. Lu, *Sol. RRL*, 2020, **4**, 2300267.
51 C. Sun, F. Pan, H. Bin, J. Zhang, L. Xue, B. Qiu, Z. Wei, Z.-G. Zhang and Y. Li, *Nat. Commun.*, 2018, **9**, 743.
52 H. Bristow, P. Jacoutot, A. D. Scaccabarozzi, M. Babics, M. Moser, A. Wadsworth, T. D. Anthopoulos, A. Bakulin, I. Mcculloch and N. Gasparini, *ACS Appl. Mater. Interfaces*, 2020, **12**, 48836–48844.
53 F. Furlan, D. Nodari, E. Palladino, E. Angela, L. Mohan, J. Briscoe, M. J. Fuchter, T. J. Macdonald, G. Grancini, M. A. McLachlan and N. Gasparini, *Adv. Opt. Mater.*, 2022, **10**, 2201816.
54 F. N. Hooge, *IEEE Trans. Electron Devices*, 1994, **41**, 1926–1935.
55 P. E. Keivanidis, P. K. H. Ho, R. H. Friend and N. C. Greenham, *Adv. Funct. Mater.*, 2010, **20**, 3895–3903.
56 R. D. Jansen-van Vuuren, A. Armin, A. K. Pandey, P. L. Burn and P. Meredith, *Adv. Mater.*, 2016, **28**, 4766–4802.
57 N. Strobel, N. Droseros, W. Köntges, M. Seiberlich, M. Pietsch, S. Schlisske, F. Lindheimer, R. R. Schröder, U. Lemmer, M. Pfannmöller, N. Banerji and G. Hernandez-Sosa, *Adv. Mater.*, 2020, **32**, 1908258.
58 J. Huang, J. Lee, J. Vollbrecht, V. V. Brus, A. L. Dixon, D. X. Cao, Z. Zhu, Z. Du, H. Wang, K. Cho, G. C. Bazan and T. Q. Nguyen, *Adv. Mater.*, 2020, **32**, 1906027.
59 M. Babics, H. Bristow, W. Zhang, A. Wadsworth, M. Neophytou, N. Gasparini and I. Mcculloch, *J. Mater. Chem. C*, 2021, **9**, 2375–2380.
60 M. Kielar, O. Dhez, G. Pecastaings, A. Curutchet and L. Hirsch, *Sci. Rep.*, 2016, **6**, 39201.
61 P. N. Murgatroyd, *Journal of physics. D, Appl. Phys.*, 1970, **3**, 151–156.
62 G. Lakhwani, A. Rao and R. H. Friend, *Annu. Rev. Phys. Chem.*, 2014, **65**, 557–581.
63 H. Cha, Y. Zheng, Y. Dong, H. H. Lee, J. Wu, H. Bristow, J. Zhang, H. K. H. Lee, W. C. Tsoi, A. A. Bakulin, I. Mcculloch and J. R. Durrant, *Adv. Energy Mater.*, 2020, **10**, 2001149.
64 Y. Tamai, Y. Fan, V. Kim, K. Ziabrev, A. Rao, S. Barlow, S. Marder, R. Friend and S. Menke, *ACS Nano*, 2017, **11**, 12473–12481.
65 C. Fuentes-Hernandez, W. Chou, T. Khan, L. Diniz, J. Lukens, F. Larrain, V. Rodriguez-Toro and B. Kippelen, *Science*, 2020, **370**, 698.
66 Y. Lau, Z. Lan, L. Cai and F. Zhu, *Mater. Today Energy*, 2021, **21**, 100708.
67 S. Gélinas, Doctor of Philosophy (PhD), University of Cambridge, 2013.